



Original Article

Development of a drift-flux model based core thermal-hydraulics code for efficient high-fidelity multiphysics calculation

Jaejin Lee, Alberto Facchini, Han Gyu Joo*

Seoul National University, 1 Gwanak-ro, Gwanak-gu, Seoul, 08826, Republic of Korea



ARTICLE INFO

Article history:

Received 19 February 2019

Received in revised form

26 March 2019

Accepted 2 April 2019

Available online 9 April 2019

Keywords:

Drift-flux model

Reactor core thermal-hydraulics

Subchannel analysis

Massively parallel execution

SIMPLEC

ABSTRACT

The methods and performance of a pin-level nuclear reactor core thermal-hydraulics (T/H) code ESCOT employing the drift-flux model are presented. This code aims at providing an accurate yet fast core thermal-hydraulics solution capability to high-fidelity multiphysics core analysis systems targeting massively parallel computing platforms. The four equation drift-flux model is adopted for two-phase calculations, and numerical solutions are obtained by applying the Finite Volume Method (FVM) and the Semi-Implicit Method for Pressure-Linked Equation (SIMPLE)-like algorithm in a staggered grid system. Constitutive models involving turbulent mixing, pressure drop, and vapor generation are employed to simulate key phenomena in subchannel-scale analyses. ESCOT is parallelized by a domain decomposition scheme that involves both radial and axial decomposition to enable highly parallelized execution. The ESCOT solutions are validated through the applications to various experiments which include CNEN 4 × 4, Weiss et al. two assemblies, PNNL 2 × 6, RPI 2 × 2 air-water, and PSBT covering single/two-phase and unheated/heated conditions. The parameters of interest for validation include various flow characteristics such as turbulent mixing, spacer grid pressure drop, cross-flow, reverse flow, buoyancy effect, void drift, and bubble generation. For all the validation tests, ESCOT shows good agreements with measured data in the extent comparable to those of other subchannel-scale codes: COBRA-TF, MATRA and/or CUPID. The execution performance is examined with a mini-sized whole core consisting of 89 fuel assemblies and for an OPR1000 core. It turns out that it is about 1.5 times faster than a subchannel code based on the two-fluid three field model and the axial domain decomposition scheme works as well as the radial one yielding a steady-state solution for the OPR1000 core within 30 s with 104 processors.

© 2019 Korean Nuclear Society, Published by Elsevier Korea LLC. This is an open access article under the CC BY-NC-ND license (<http://creativecommons.org/licenses/by-nc-nd/4.0/>).

1. Introduction

As the computing technology is continuously enhanced, numerical solutions with higher resolutions and fewer approximations become more affordable. In nuclear reactor analyses, pin-resolved whole core multiphysics calculations take the advantages of such highly enhanced computing technology. In particular, pin-level neutronics and thermal-hydraulics (T/H) coupled calculations have been carried out by numerous institutions to incorporate their strong interdependencies [1–3]. The effectiveness of such pin-level coupled analysis was proved with accurate predictions of core depletion [1] and CRUD-induced power shift (CIPS) [4] phenomena. In these coupled calculations, the T/H solver plays a key role in providing the accurate temperature and density distributions of the coolant and fuel.

Even though researches for coupling a Computational Fluid Dynamics (CFD) code with a neutronics code [5,6] had been performed, there is a strong demand for subchannel-scale T/H codes in the multiphysics coupling because of their adequacy in terms of speed and accuracy. COBRA-TF (CTF) [7] is one of the well-known subchannel analysis codes. The two-fluid three field model is used to form the governing equations. CTF solves the pressure correction equations for the whole problem domain as the Semi-Implicit Pressure Linked Equation (SIMPLE) method [8] does. The excellent performance of the code and its well-established coupling interface resulted in coupling with many neutronics codes such as MPACT [9], TORT-TD [10], and nTRACER [11]. On the other hand, Korea Atomic Energy Research Institution (KAERI) has been trying to apply its component scale T/H analysis code CUPID [12] to sub-channel analyses [13]. The CUPID code adopts a three-dimensional (3-D) two-fluid model, collocated meshing, and the Implicit Continuous Eulerian (ICE) method. Subchannel models related to pressure drop and turbulent mixing are implemented in CUPID to extend its applicability to subchannel-scale analyses. The DeCART/

* Corresponding author.

E-mail address: johan@snu.ac.kr (H.G. Joo).

Nomenclature		<i>Greek letter</i>
A_c	Flow area of channel	α Void fraction
D_h	Hydraulic diameter	β Turbulent mixing coefficient
f	Darcy friction factor	Γ Vapor generation rate
G	Mass flux	Θ Turbulent mixing two-phase multiplier
g	Gravity acceleration	ρ Density
H	Heat transfer coefficient	τ Shear stress
h	Enthalpy	Φ Two-phase multiplier
P	Pressure	
T	Temperature	
u	Velocity	
x	Flow quality	
		<i>Subscript</i>
		l Liquid phase
		m Mixture
		tm Turbulent mixing and void drift
		v Vapor phase
		w Wall

CUPID coupled system [14] was established through a socket communication with TCP/IP.

MATRA [15] is another subchannel code of KAESI having a lot different features. It is specialized to simulating the cores that have a dominating flow direction. By adopting the Homogeneous Equilibrium Model (HEM) and the space-marching scheme, MATRA achieves significant computing-time-saving so that it could have been used widely for various core thermal designs and for the evaluation of Departure from Nucleate Boiling Ratio (DNBR) margins. The slip model and the explicit scheme are implemented in order to handle more complicated conditions involving considerable phase change or reverse flow. The coupling of MATRA with neutronics codes has been done by various institutions as well [16,17].

Even though many existing subchannel codes are well-designed and show excellent performance, most of them do not use the drift-flux model (DFM) [18] for the governing equations to handle two-phase flow. In general, the DFM has been widely used in system analysis codes [19,20] because it could show the best applicability in 1-D problems. Nonetheless, some subchannel codes [21,22], which were developed more than 30 years ago, adopted the DFM in 3-D domains. The effectiveness of the DFM was demonstrated in these codes in terms of sufficient accuracy and considerable time-saving in the comparison with the two-fluid model and the HEM. However, parallel execution was not the concern in these codes.

It is known that the DFM produces sufficiently accurate solutions for most of the core T/H conditions excluding highly voided conditions in which the neutronic feedback effect is not important in pressurized water reactors (PWRs). It is thus worthwhile to adopt the DFM rather than the two-fluid model for core T/H calculations to achieve high speed execution. In this regard, the development of a new subchannel scale core T/H code called ESCOT (Efficient Simulator of Core Thermal-hydraulics) was initiated at Seoul National University as an effort to provide efficient core T/H solutions to multiphysics analysis systems targeting high-performance parallel computing platforms. The code is based on the four-equation DFM and the SIMPLEC (SIMPLE-Consistent) method. It is parallelized by employing both radial and axial domain decomposition with the Message Passing Interface (MPI) library.

In the following, the overall numerical schemes and models implemented in ESCOT will be presented first. The validation of the solution capability will then be demonstrated with five problems covering unheated/heated single-/two-phase flow conditions. It includes the comparisons with measured data and also with the results of other codes such as CTF, MATRA and CUPID. Finally, the execution performance of ESCOT will be assessed for a whole core problem having 89 fuel assemblies and for a quarter core problem

of a Korean PWR.

2. Numerical solution schemes and features of ESCOT

The four-equation DFM is employed for setting up the governing equations of ESCOT. It assumes the saturation condition for the vapor phase. It is augmented by several constitutive relations such as pressure drop and turbulent mixing relations. The governing equations, the constitutive relations, and the numerical solution scheme characterized by the SIMPLE method are presented in this section. The standard symbols and notations which are clarified in the nomenclature section will be used throughout the paper.

2.1. Governing equations

The mixture mass conservation equation is given as:

$$\frac{\partial \rho_m}{\partial t} + \nabla \cdot (\rho_m \vec{u}_m) = -\nabla \cdot \vec{W}_{tm}'' \quad (1)$$

where the mixture density and velocity are defined as follows:

$$\rho_m = \alpha \rho_v + (1 - \alpha) \rho_l \quad (2)$$

and

$$\vec{u}_m = \frac{\alpha \rho_v \vec{u}_v + (1 - \alpha) \rho_l \vec{u}_l}{\rho_m} \quad (3)$$

The subscripts, m , l and v denote mixture, liquid, and vapor phase, respectively. The term on the right-hand-side (RHS) indicates the mass exchange due to turbulent mixing.

The vapor mass conservation equation is given as:

$$\frac{\partial (\alpha \rho_v)}{\partial t} + \nabla \cdot (\alpha \rho_v \vec{u}_m) = \Gamma_v''' - \nabla \cdot \vec{W}_{tm,v}''' - \nabla \cdot \left(\frac{\alpha \rho_l \rho_v \vec{V}'_{gj}}{\rho_m} \right) \quad (4)$$

where the two divergence terms on the RHS represent vapor exchange by turbulent mixing and by the characteristics of the DFM, respectively.

The mixture momentum conservation equation is then given as:

$$\begin{aligned} \frac{\partial (\rho_m \vec{u}_m)}{\partial t} + \nabla \cdot (\rho_m \vec{u}_m \vec{u}_m) &= \rho_m \vec{g} - \nabla P + \nabla \cdot \vec{F}_m^{ij} - \nabla \cdot \vec{F}_{tm}'' \\ &- \nabla \cdot \left(\frac{\alpha}{1 - \alpha} \frac{\rho_v \rho_l}{\rho_m} \vec{V}'_{gj} \vec{V}'_{gj} \right) \end{aligned} \quad (5)$$

where the terms of the RHS are the body force, force by pressure gradient, friction force, momentum exchange by turbulent mixing, and the divergence term by the DFM.

The energy conservation equation is formulated in terms of mixture enthalpy as:

$$\frac{\partial(\rho_m h_m)}{\partial t} + \nabla \cdot (\rho_m h_m \vec{u}_m) = q''_w + q'''_v - \nabla \cdot \vec{Q}_{tm}'' + \frac{\partial P}{\partial t} - \nabla \cdot \left(\frac{\alpha \rho_v \rho_l}{\rho_m} (h_v - h_l) \vec{V}'_{gj} \right) \quad (6)$$

where the mixture enthalpy is defined as:

$$h_m = \frac{\alpha \rho_v h_m + (1 - \alpha) \rho_l h_m}{\rho_m}. \quad (7)$$

The terms on the RHS represent the energy transfer rate from heated walls, volumetric heat generation rate in the fluid, energy exchange by turbulent mixing, work done by pressure, and the divergence term by the DFM.

2.2. Constitutive relations

In order to close the four equations which have a lot more independent variables than the number of equations, several constitutive relations are required starting from the equation of state. Particularly, the relations for drift-flux parameters and a turbulent mixing model should be provided based on experimental data. The constitutive relations used in ESCOT are given below.

2.2.1. Equation of state

The primary variables in the above equations are pressure, void fraction, liquid enthalpy, and mixture velocity. The secondary variables would be calculated by using the Equation of State. The IAPWS-IF97 steam table of CTF [7] is used in ESCOT. The liquid density can then be obtained as:

$$\rho_l = \rho_l(P, h_l). \quad (8)$$

Under the assumption that vapor is in the saturated condition, all the variables for the vapor phase are determined by pressure only as:

$$T_v = T_{sat}(P) \quad (9)$$

and

$$\rho_v = \rho_{v,sat}(P). \quad (10)$$

2.2.2. Drift-flux parameters

The distribution parameter C_0 and the gas drift velocity V'_{gj} , which are so called the drift-flux parameters, play a key role in predicting the gas and liquid velocities from the mixture velocity as follows:

$$V'_{gj} = \frac{\rho_m V'_{gj} + \rho_m (C_0 - 1) u_m}{\rho_m - (C_0 - 1) \alpha (\rho_l - \rho_g)}, \quad (11)$$

$$u_l = u_m - \frac{\alpha}{1 - \alpha} \frac{\rho_v}{\rho_m} V'_{gj} \quad (12)$$

and

$$u_v = u_m + \frac{\rho_l}{\rho_m} V'_{gj}. \quad (13)$$

In general, the drift-flux parameters are given as a function of several factors as:

$$C_0 = C_0(\alpha, \rho_l, \rho_v, \dots) \quad (14)$$

and

$$V'_{gj} = V'_{gj}(\alpha, \rho_l, \rho_v, g, \sigma, \dots). \quad (15)$$

Various correlations are suggested for these functions and the applicable range of a model has to be carefully limited considering the flow regime map, pressure, flow velocity, and flow orientation to guarantee the validity of the solutions. Two models are implemented in ESCOT, the Zuber and Findlay correlation [18] and the Chehal-Lelloche correlation [23], so that the user can select a model with an input option.

2.2.3. Pressure drop model

The pressure drop models are implemented to incorporate friction and form loss as follows:

$$\begin{aligned} \nabla \cdot \tau_m^{ij} &= - \left(\frac{dP}{dX} \Big|_{friction} + \frac{dP}{dX} \Big|_{form} \right) \\ &= -\Phi \left(\sum_k \frac{f_k}{2D_h} \frac{G_k |G_k|}{\rho_k} + \frac{K_x}{2\Delta x} \rho_m u_m |u_m| + \frac{K_z}{2\Delta z} \rho_m u_m |u_m| \right) \end{aligned} \quad (16)$$

where the subscript k indicates the phase, liquid or vapor. f is the friction factor while K is the form loss factor and Φ is the two-phase multiplier. In the case of friction, the term is applied to the axial direction which is the major direction in subchannel analyses. The friction factor is a function of Reynolds number, and can be expressed as follows:

$$f_k = a \text{Re}_k^b + c. \quad (17)$$

The parameters in Eq. (17) are given differently according to the flow condition which can be characterized by Reynolds number as shown in Table 1.

The Reynolds number for each phase is defined as [24]:

$$\text{Re}_k = \frac{\alpha_k \rho_k u_k}{\mu_m} \quad (18)$$

where the mixture viscosity is obtained as:

$$\mu_m = \left[\frac{1 - x}{\mu_l} + \frac{x}{\mu_v} \right]^{-1}. \quad (19)$$

The form loss term would influence the flow which moves toward the axial and lateral directions. Generally, the axial form loss occurs due to the existence of spacer grids while the lateral form loss is caused by the flow passing through two rods.

In order to take into account the effect of two-phase flow on pressure drop, the two-phase multiplier proposed by Armand [25]

Table 1
Friction factor parameters at different flow conditions.

Flow condition	a	b	c	Applicable range
Laminar	64.0	-1.0	0	$\text{Re} < 2300$
Transition	0.316	-0.25	0	$2300 \leq \text{Re} < 30,000$
Turbulent	0.184	-0.20	0	$30,000 \leq \text{Re}$

is applied.

2.2.4. Turbulent mixing model

The mass, momentum, and energy of the flow in one cell are mixed with those of the neighboring cells by not only cross-flow created by pressure gradient but also by turbulent mixing and void drift. The latter two phenomena competitively affect the flow. In the case of turbulent mixing, the flow gains its quantity from the neighboring cells that have larger values. Or the flow loses its quantity by spreading it to the neighboring cells that have smaller values. Thus, turbulent mixing contributes to generating an even distribution of the three physical quantities. The void drift, however, works in the opposite way. For example, small bubbles gather and form larger bubbles so that the nonuniformity of the bubble distribution increases.

In subchannel codes, these physical phenomena are usually incorporated by either the Equal Volume exchange and Void Drift (EVVD) model [26] or the Equal Mass exchange and Void Drift (EMVD) model. In ESCOT, the EVVD model is implemented into the governing equations in the following form:

Mixture mass exchange:

$$\begin{aligned} \nabla \cdot \vec{W}_{tm}'' &= \sum_j \frac{s_{ij}}{A_i} (W_{tm}''^{TM} + W_{tm}''^{VD}) \\ &= \sum_j \frac{s_{ij}}{A_i} \Theta_{ij} \frac{\epsilon}{z_{ij}^T} \left[\left\{ (\rho_m)_i - (\rho_m)_j \right\} - \left\{ K_m \frac{G_i - G_j}{G_i + G_j} ([\alpha(\rho_v - \rho_l)]_i \right. \right. \\ &\quad \left. \left. + [\alpha(\rho_v - \rho_l)]_j) \right\} \right]. \end{aligned} \quad (20)$$

Vapor mass exchange:

$$\begin{aligned} \nabla \cdot \vec{W}_{tm,v}'' &= \sum_j \frac{s_{ij}}{A_i} (W_{tm,v}''^{TM} + W_{tm,v}''^{VD}) \\ &= \sum_j \frac{s_{ij}}{A_i} \Theta_{ij} \frac{\epsilon}{z_{ij}^T} \left[\left\{ (\alpha\rho_v)_i - (\alpha\rho_v)_j \right\} - \left\{ K_m \frac{G_i - G_j}{G_i + G_j} ((\alpha\rho_v)_i + (\alpha\rho_v)_j) \right\} \right]. \end{aligned} \quad (21)$$

Momentum exchange:

$$\begin{aligned} \nabla \cdot \vec{F}_{tm}'' &= \sum_j \frac{s_{ij}}{A_i} (F_{tm}''^{TM} + F_{tm}''^{VD}) \\ &= \sum_j \frac{s_{ij}}{A_i} \Theta_{ij} \frac{\epsilon}{z_{ij}^T} \left[\left\{ (\rho_m u_m)_i - (\rho_m u_m)_j \right\} \right. \\ &\quad \left. - \left\{ K_m \frac{G_i - G_j}{G_i + G_j} ([\alpha(\rho_v u_v - \rho_l u_l)]_i + [\alpha(\rho_v u_v - \rho_l u_l)]_j) \right\} \right] \end{aligned} \quad (22)$$

Energy exchange:

$$\begin{aligned} \nabla \cdot \vec{Q}_{tm}'' &= \sum_j \frac{s_{ij}}{A_i} (Q_{tm}''^{TM} + Q_{tm}''^{VD}) \\ &= \sum_j \frac{s_{ij}}{A_i} \Theta_{ij} \frac{\epsilon}{z_{ij}^T} \left[\left\{ (\rho_m h_m)_i - (\rho_m h_m)_j \right\} \right. \\ &\quad \left. - \left\{ K_m \frac{G_i - G_j}{G_i + G_j} ([\alpha(\rho_v h_v - \rho_l h_l)]_i + [\alpha(\rho_v h_v - \rho_l h_l)]_j) \right\} \right] \end{aligned} \quad (23)$$

ϵ here is eddy diffusivity, and z^T is turbulent mixing length. K_m

denotes the scaling factor whose typical value is taken to be 1.4. It can be flexibly assigned by the user. The mixing coefficient can be reformulated as a function of mass flux [7] as:

$$\frac{\epsilon}{z_{ij}^T} = \frac{\beta \bar{G}}{\rho}. \quad (24)$$

The value of the turbulent mixing coefficient β is provided by the user. In the case of the two-phase multiplier Θ , the model proposed by Beus [27] is used.

2.2.5. Flow regime map and vapor generation rate

The vertical flow regime map of RELAP5-3D [28] is used to determine the flow regimes of ESCOT. Because ESCOT assumes saturated conditions for the vapor phase, the flow regimes for the pre-Critical Heat Flux (CHF) range are considered: bubbly flow, slug flow, the transition between slug and annular mist flows, and annular mist flow. The flow regimes help ESCOT to use proper correlations of the DFM and the interfacial heat transfer coefficient.

The model for the vapor generation term I_v''' in RELAP5-3D is also adopted to complete the constitutive correlations. It consists of a summation of the two terms as in Eq. (25) which are the volumetric vapor generation rate by heated walls I_w''' and the volumetric vapor exchange term through the interface of two-phase I_{iv}''' :

$$I_v''' = I_w''' + I_{iv}''' \quad (25)$$

The near wall region volumetric vapor generation rate is calculated by the following correlation of Lahey [29] which specifies subcooled boiling that occurs when the liquid enthalpy becomes higher than the critical enthalpy.

The interfacial vapor exchange term under the saturated vapor assumption is given as:

$$I_{iv}''' = \frac{H_{iv}(T_v - T_{sat}) + H_{il}(T_l - T_{sat})}{h_{vi} - h_{il}} = \frac{H_{il}(T_l - T_{sat})}{h_{v,sat} - h_{il}} \quad (26)$$

with

$$h_{il} = \begin{cases} h_l & \text{if } T_l > T_{sat} (\text{vaporization}) \\ h_{l,sat} & \text{if } T_l \leq T_{sat} (\text{condensation}) \end{cases}$$

Here the interfacial heat transfer coefficient H_{il} depends on the flow regime map and the correlations of RELAP-3D are applied as well [28].

2.3. Numerical solution methods

The governing equations are spatially discretized by the Finite Volume Method (FVM) employing a staggered grid structure. The semi-implicit method is applied for temporal discretization. The pressure correction equation is derived by the SIMPLEC (SIMPLE-Consistent) [30] scheme.

2.3.1. Discretization

Because the basic geometry for the application of ESCOT would be square lattices which are typical in Light Water Reactors (LWRs), the staggered grid structure would be adequate. Fig. 1 shows the staggered grid of ESCOT. The scalar variables such as pressure, enthalpy, and density are defined at subchannel-centered scalar cells while the mixture velocity is defined at the gap-centered momentum cells. The drift-flux parameter V'_{gj} which is a function of the drift parameter and gas drift velocity is also defined at the momentum cell because its characteristic is analogous to that of velocity. In the following descriptions, the subscripts I and J denote the radial and axial indices of the scalar cells, respectively, and the

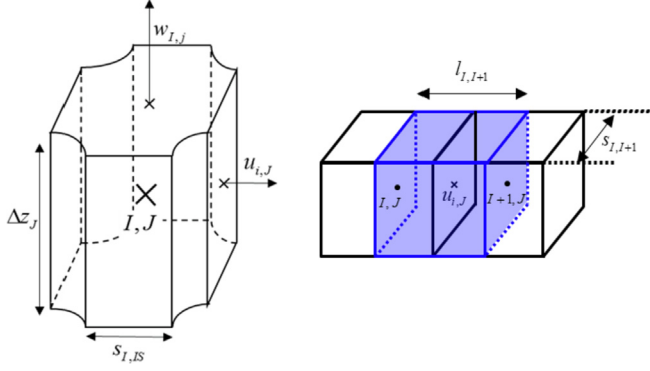


Fig. 1. Schematic drawing of a scalar cell and momentum cell in the staggered grid.

subscripts i and j are those of the momentum cells.

The surface values of a control volume are determined by the donor cell scheme as follows:

$$\phi_{I,J}^n = \begin{cases} \phi_{I,J}^n & \text{if } u_{i,J}^n \geq 0 \\ \phi_{I+1,J}^n & \text{if } u_{i,J}^n < 0 \end{cases} \quad (27)$$

where n is the time step index. A weighted average is applied when the cell-centered values of surface quantities are necessary. This harmonic average is given as:

$$\phi_{I,J}^n = \frac{\Delta z_{J+1} \phi_{I,J}^n + \Delta z_J \phi_{I,J+1}^n}{\Delta z_J + \Delta z_{J+1}}. \quad (28)$$

The temporal discretization is based on the semi-implicit scheme. In this scheme, the sonic propagation and interphase exchange such as pressure and interfacial temperature are treated implicitly because their physical phenomena occur in a relatively short time. On the other hand, the terms related with fluid convection which would allow relatively larger timescales are treated explicitly. For example, the interfacial mass exchange term, which is a source term of the vapor continuity equation, can be written as:

$$\int_{CV} \Gamma_{iv}''' dV = \frac{H_{il,IJ}^n [(T_l)_{IJ}^{n+1} - (T_{sat})_{IJ}^{n+1}]}{(h_{v,sat})_{IJ}^n - (h_{il})_{IJ}^n} \Delta V_{IJ}. \quad (29)$$

The turbulent mixing terms are implemented in a hybrid way such that the turbulent mixings of mass and energy are treated explicitly and the momentum turbulent mixing term is moved to LHS for the implicit treatment.

The following is a discretized mixture continuity equation given as an example in a simplified form for the sake of demonstration:

$$\frac{\rho_{m,IJ}^{n+1} - \rho_m^n}{\Delta t} \Delta V + \sum \rho_m^n (\vec{u}_m^{n+1} \cdot \vec{n}) A = \sum W_{tm}^n. \quad (30)$$

2.3.2. Derivation of the pressure correction equation and the calculation procedure

The SIMPLEC algorithm is adopted to establish the pressure correction equation over the entire problem domain [30]. The relation between the next time step velocity and pressure correction can be formulated in SIMPLEC as follows:

$$w_{m,IJ}^{n+1} = w_{m,IJ}^* + d_{IJ} \left[(P_{IJ}^{n+1} - P_{IJ}^*) - (P_{IJ+1}^{n+1} - P_{IJ+1}^*) \right] \quad (31)$$

where

$$d_{IJ} = \frac{A_{IJ}}{a_{z,P} - \sum_{nb} a_{z,nb}} \quad (32)$$

and $a_{z,P}$ and $a_{z,nb}$ are the diagonal and off-diagonal terms of discretized axial momentum equation, respectively. The superscript * denotes the intermediate solution. The above relation must be coupled with scalar equations, Eqs. (1), (4), and (6), to yield the pressure correction equation which would close the governing equations. There are numerous ways to derive it, and we choose the way to couple all scalar equations. First, the secondary variables in scalar equations are linearized as a function of primary variables as follows:

$$T_l^{n+1} = T_l^n + (P^{n+1} - P^n) \left(\frac{\partial T_l}{\partial P} \right)^n + (h_l^{n+1} - h_l^n) \left(\frac{\partial T_l}{\partial h_l} \right)^n. \quad (33)$$

It leads to the following element of the coupled linear system for certain scalar cell (I,J) with the discretized scalar equations:

$$\begin{bmatrix} a_{11} & a_{12} & a_{13} \\ a_{21} & a_{22} & a_{23} \\ a_{31} & a_{32} & a_{33} \end{bmatrix} \begin{bmatrix} h_{I,J}^{n+1} \\ \alpha_{I,J}^{n+1} \\ P_{I,J}^{n+1} \end{bmatrix} = \begin{bmatrix} s_1 \\ s_2 \\ s_3 \end{bmatrix} - \begin{bmatrix} b_{11} & b_{12} & b_{13} & b_{14} & b_{15} & b_{16} \\ b_{21} & b_{22} & b_{23} & b_{24} & b_{25} & b_{26} \\ b_{31} & b_{32} & b_{33} & b_{23} & b_{35} & b_{36} \end{bmatrix} \times \begin{bmatrix} u_{ie,J}^{n+1} \\ -u_{iw,J}^{n+1} \\ v_{is,J}^{n+1} \\ -v_{in,J}^{n+1} \\ w_{I,J}^{n+1} \\ -w_{I,J-1}^{n+1} \end{bmatrix}. \quad (34)$$

By replacing the velocities of the new time step ($n+1$) in Eq. (34) with Eq. (31) and by inverting the 3×3 coefficient matrix on the LHS, the following linear system can be derived:

$$\begin{bmatrix} h_{I,J}^{n+1} \\ \alpha_{I,J}^{n+1} \\ P_{I,J}^{n+1} \end{bmatrix} = \begin{bmatrix} s'_1 \\ s'_2 \\ s'_3 \end{bmatrix} - \begin{bmatrix} b'_{11} & b'_{12} & b'_{13} & b'_{14} & b'_{15} & b'_{16} \\ b'_{21} & b'_{22} & b'_{23} & b'_{24} & b'_{25} & b'_{26} \\ b'_{31} & b'_{32} & b'_{33} & b'_{34} & b'_{35} & b'_{36} \end{bmatrix} \times \begin{bmatrix} d_{ie,J} [P_{IJ}^{n+1} - P_{IEJ}^{n+1}] \\ d_{iw,J} [P_{IJ}^{n+1} - P_{IWJ}^{n+1}] \\ d_{is,J} [P_{IJ}^{n+1} - P_{ISJ}^{n+1}] \\ d_{in,J} [P_{IJ}^{n+1} - P_{INJ}^{n+1}] \\ d_{I,J} [P_{IJ}^{n+1} - P_{IJ+1}^{n+1}] \\ d_{I,J-1} [P_{IJ}^{n+1} - P_{IJ-1}^{n+1}] \end{bmatrix}. \quad (35)$$

Note that the linear system is changed to have neighbor coupling only in terms of pressure. Finally, extracting the 3rd row yields the linear system for the pressure equation as:

$$\left[1 + \sum_{nb} b''_{nb} \right] P_{IJ}^{n+1} - \sum_{nb} b''_{nb} P_{nb}^{n+1} = s'_3. \quad (36)$$

The coefficient matrix of the linear system is septa-diagonal and its diagonal dominance is very weak because the diagonal entry is greater than the summation of the off-diagonal elements by only unity and the off-diagonal entries are much greater than unity. Because of the weak diagonal dominance and the sparseness of the pressure matrix, it is not recommended to use a traditional iterative

method. Instead, the Krylov Subspace Methods (KSM) are used as effective solvers [31]. In ESCOT, the PETSc solver [32] as well as a built-in BiCGSTAB solver are implemented so that various KSMs are available for user's choice.

The overall calculation procedure of ESCOT is illustrated in Fig. 2. At the beginning of a calculation, the flow regime maps in all computing cells are determined to select proper correlations. The intermediate velocities are then obtained by solving the linear systems of lateral and axial momentum equations, which are a penta-diagonal and a septa-diagonal matrix, respectively. Next, the linear system of the pressure equation is solved, and the mixture velocity at the new time step is updated by the solution of the pressure equation. In fact, outer iterations would be recommended to achieve the converged solutions of velocities and pressure, but performing only one outer iteration turned out to be enough in most cases as long as the time step size is sufficiently small. The rest primary variables are determined by solving the linear system of Eq. (34). The secondary variables are then updated through the steam table. The calculation is terminated when the convergence criteria are met or the simulation time reaches the end time.

2.4. Parallel calculation scheme

The ESCOT code aims at highly parallelized execution. A multi-node and multiprocessor system is a target computing environment of the code. In a previous research [33], it was figured out that when the radial domain decomposition is applied at the assembly

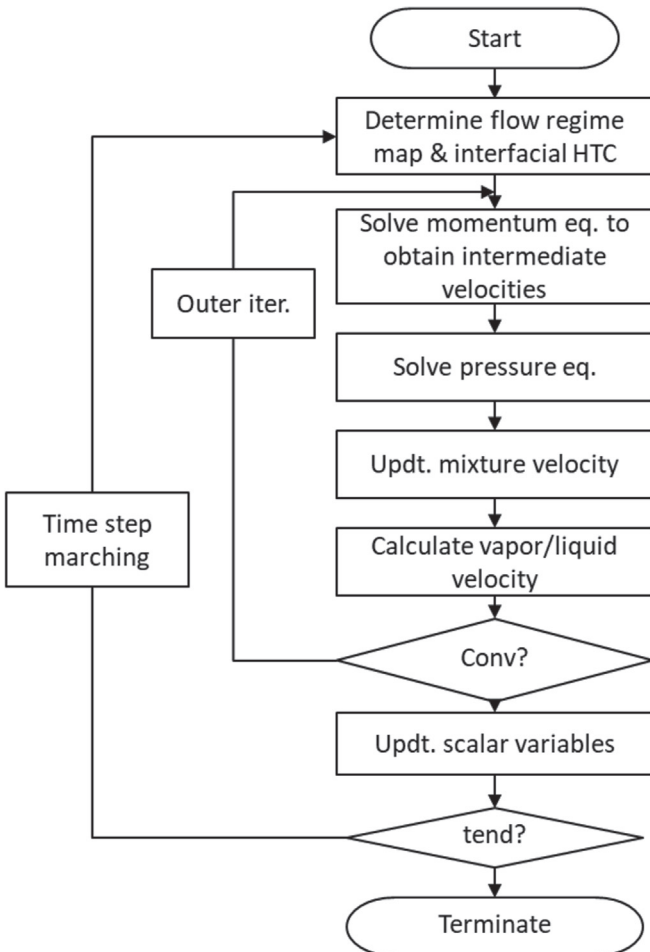


Fig. 2. Flowchart of ESCOT based on the SIMPLEC Algorithm.

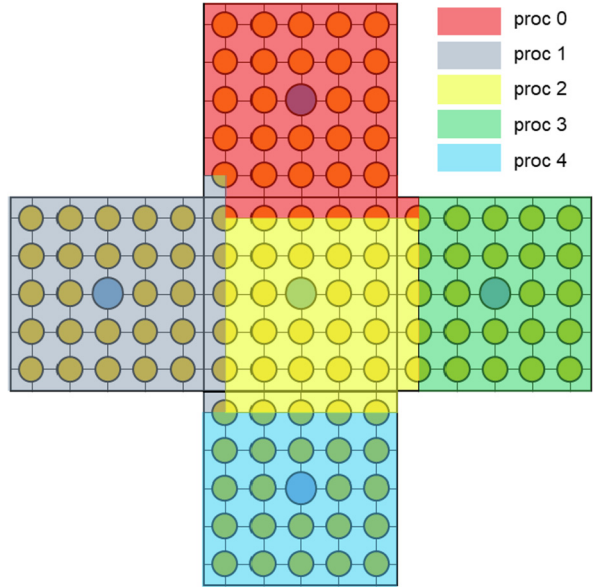


Fig. 3. Example of assembly-wise radial decomposition in ESCOT

or sub-assembly level in a subchannel code, satisfactory parallel performance could be obtainable with MPI parallelization. Thus ESCOT is also parallelized with MPI. Unlike CTF, however, the problem domains are decomposed not only radially, but also axially. Assembly-wise domain decomposition is used radially as shown in Fig. 3 which indicates subdomains with different colors.

It should be noted that ghost cells are assigned near the boundary of a subdomain. The role of the ghost cells is to provide the boundary information of the neighboring subdomains, which is required to solve the problem for the local subdomain. The example of assigning the ghost cells are illustrated in Fig. 4 and Fig. 5.

The parallel execution of ESCOT proceeds as follows. First, the code produces converged local solutions of the primary variables at the current time step by solving three linear systems. The primary variables include pressure, liquid enthalpy, void fraction, and mixture velocity. Secondly, the local primary solutions that are adjacent to neighboring domains are transmitted to their ghost cells through the MPI communication. Finally, the rest of the properties in the local cells and ghost cells are locally updated through the steam table or the drift-flux correlations. In this way, the code could have synchronous solutions at the time step.

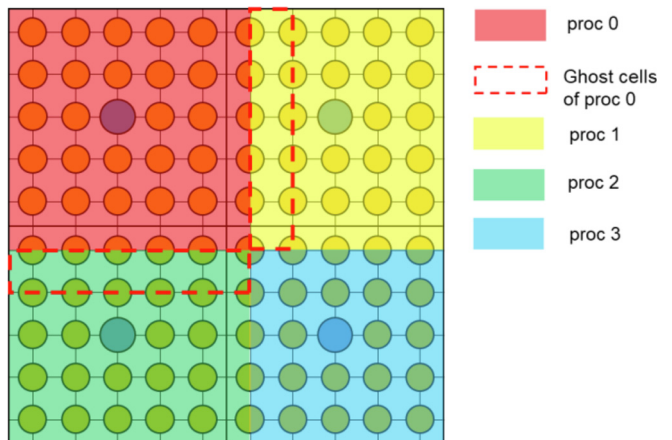


Fig. 4. Assignment of ghost scalar cells.

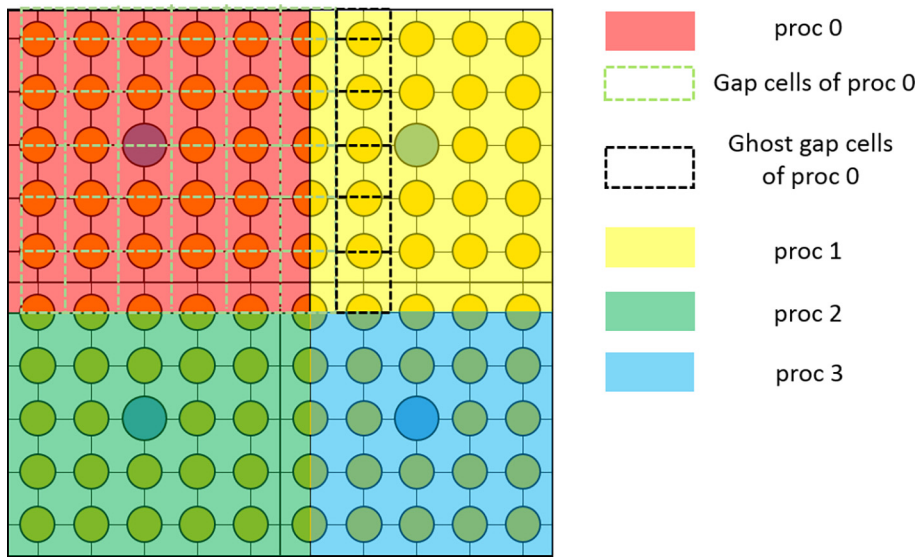


Fig. 5. Assignment of ghost momentum cells.

3. Validation of ESCOT

In order to verify the solution accuracy of ESCOT, a set of flow experiments were analyzed by ESCOT and the solutions were compared to the experiment data and the results of three other subchannel-scale codes: CTF [34], MATRA [15], and/or CUPID [13].

Firstly, three single-phase validation results consisting of two unheated test cases and one heated test case are presented. Through the CNEN 4×4 test [35], the models for momentum turbulent mixing and pressure drop by spacer grid are be verified under unheated single-phase conditions. The Weiss et al. two 14×14 assembly test [36] is for the assessment of the capability to predict the flow redistribution when the cross flow is a major driving force. For the single-phase heated problem, the PNNL 2×6 test [37] is used and the buoyancy effect under a non-uniform power distribution is examined.

Secondly, two additional validation results consisting of one unheated test case and one heated test case are presented to verify the two-phase models employed in ESCOT. The void drift model is verified through the RPI 2×2 air-water mixing test [38] which is the unheated two-phase problem. The overall boiling models are verified through the PWR Sub-channel and Bundle Tests (PSBT) [39] Phase 1 – Exercise 2 (Steady-state bundle benchmark).

3.1. Single-phase flow cases

3.1.1. CNEN 4×4 test

The CNEN 4×4 experiment was performed by V. Marinelli et al. at Studsvik to produce the velocity profiles under cold single-phase flow conditions and flow redistribution between subchannels. The experimental data are used to verify the momentum turbulent mixing model and the pressure drop model for spacer grids.

The test section has a square-geometry with 16 (4×4) rods with the radial configuration shown in Fig. 6. The height is 1.4 m and a spacer grid is located at the middle of the test facility (0.7 m). The experiment was carried out without heating at five different inlet velocity conditions: 0.64, 1.32, 2.61, 3.83, and 5.18 m/sec. The outlet velocities at each subchannel were measured.

The test facility is discretized with 1250 meshes consisting of 25 (5×5) radial meshes and uniformly discretized 50 axial meshes. The outlet pressure and the inlet temperature are set to 0.10136 MPa and 300 K, respectively. The form loss factor of the

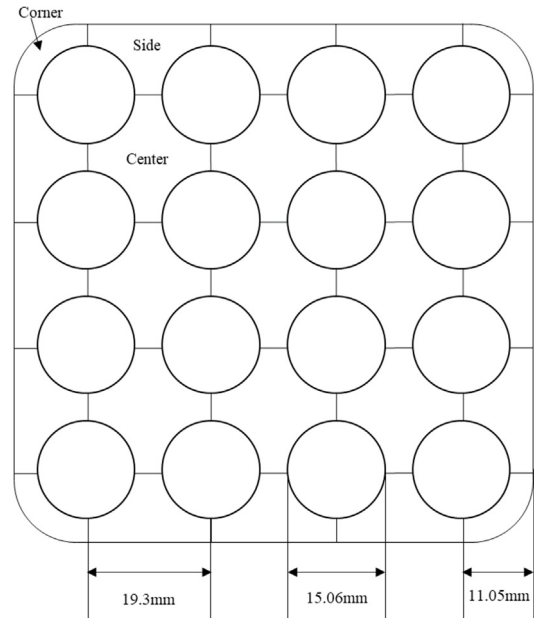


Fig. 6. Cross-sectional view of the CNEN 4×4 test facility.

spacer grid is set to 0.3.

Firstly, the pressure results are demonstrated in Fig. 7 along with the results of CUPID and MATRA. Because the experimental data of pressure are not provided, the calculated values of MATRA, CUPID, and ESCOT are compared. All three codes yielded noticeable pressure drop due to the spacer grid. The largest drop occurs for the case of the fastest inlet velocity. The maximum difference in pressure between ESCOT and other codes is 1.6% so that it can be concluded that the pressure drop models work properly.

Secondly, the calculated outlet velocities are compared with the measured data. The result given in Fig. 8 presents the calculated velocities without applying the turbulent mixing model. Both ESCOT and CUPID codes underestimate the velocities at the corner subchannels and overestimate at center subchannels. That can be explained because the center subchannels have larger hydraulics diameters than others yielding less flow resistance. However, in reality, this is mitigated by turbulent mixing with neighboring cells,

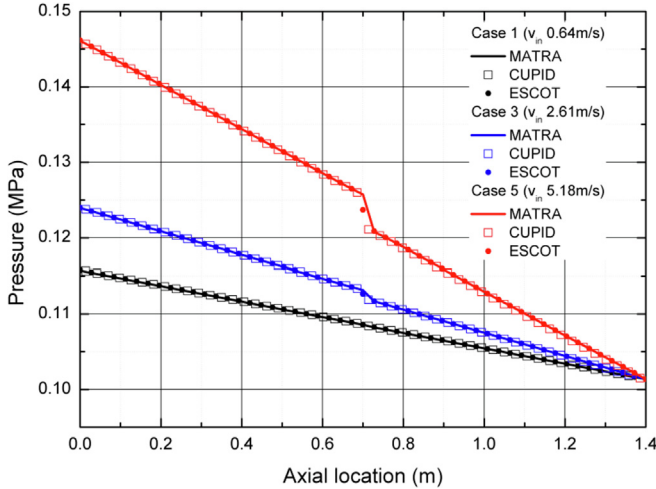


Fig. 7. Calculated pressure profile for CNEN 4 × 4.

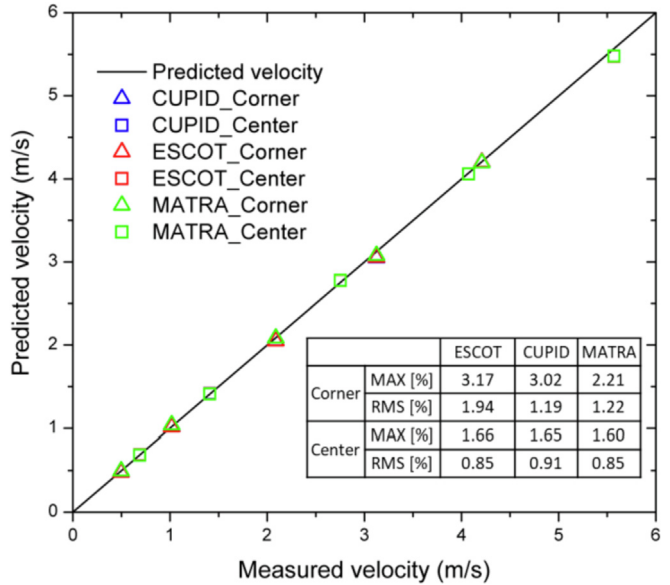


Fig. 9. Outlet velocities obtained with turbulent mixing models for CNEN 4 × 4.

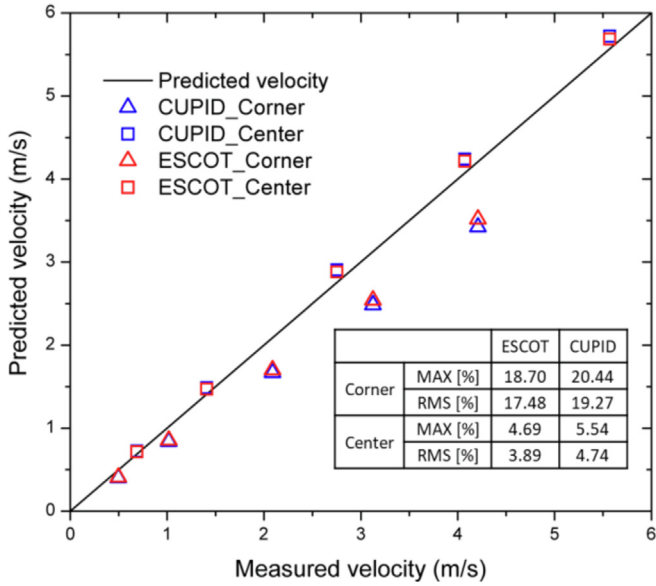


Fig. 8. Outlet velocities obtained without turbulent mixing model for CNEN 4 × 4.

and it can be taken into account with the turbulent mixing model. When the turbulent mixing coefficient β is set to 0.02, the results of three codes get closer to the measured data as shown in Fig. 9. The maximum error of ESCOT with the measured data is reduced from 18% to 3% after the turbulent mixing model is activated.

3.1.2. Weiss et al. Two 14 × 14 assembly test

The Weiss et al. two-assembly test was performed to investigate flow redistribution between two assemblies under an unheated condition when partial or full blockage occurs in one of two assemblies. The assembly of the test section consists of 14 × 14 unheated pins. The width and height of the test section are 15.33 and 7.63 inches, respectively, and the axial elevation is 38 inches. The configuration is given in Fig. 10. In order to measure velocities and static pressure, a number of pitot tubes were installed in Rows 1, 2, and 3 at seven different axial levels.

The axial problem domain is uniformly divided with 1-inch thickness so that 16,530 meshes ($29 \times 15 \times 38$) are used for the computational model. It is noted that the turbulent mixing model is deactivated, and it then means that the cross-flow is the only

driving source of the flow redistribution. The outlet pressure and the inlet temperature are set to 0.101 MPa and 299.8 K to represent the atmospheric condition.

For the partial blockage case, the inlet mass flow rates of 1100 gpm and 550 gpm were given to each assembly in the experiment. In the ESCOT calculation, the inlet velocities are set to 3.52 and 1.76 m/sec to produce the experimental mass flow rates. The inlet velocity of subchannels between two bundles is assigned as 2.64 m/sec. Fig. 11 shows the results of the flow rate fraction at each bundle obtained from ESCOT, MATRA, and CTF. ESCOT could simulate the flow redistribution by cross-flow as well as other codes did. The RMS difference from the experimental data is 2.92% that is similar to 2.05% of MATRA and 1.74% of CUPID. The flow recovery in a local view can be more clearly seen in Fig. 12. The local velocities at each level are calculated by averaging the calculated values of Rows 1, 2 and 3. Even though the local velocities of ESCOT show roughly 10% differences from the measured data, the differences are comparable to those of CUPID and MATRA. The result of ESCOT has rather small differences of 2% in the code-to-code comparison.

For the full blockage case, the inlet mass flow rates were set to 1100 gpm and 0 gpm. As shown in Fig. 13, flow recirculation could be observed by the ESCOT calculation, which is hard to simulate with a code employing a marching scheme. The local velocities at different axial levels are illustrated in Fig. 14. The velocities at low levels (1 and 2) and at the blocked side (bundle 2) are negative implying reverse flows. The flow in the blocked channel is recovered by the cross-flow as in the partial blockage case. The velocity profiles of ESCOT are similar those of CUPID. Through this analysis, the capability of ESCOT to simulate cross-flow and reverse flow is validated.

3.1.3. PNNL 2 × 6 test

The PNNL 2 × 6 test was performed by the Pacific Northwest National Laboratory to investigate the buoyancy effect due to a non-uniform power distribution. Fig. 15 is the ESCOT computational model for the PNNL test for which different power values were provided to the half of the rods. Nine windows were installed to measure velocity and temperature. Three cases with different conditions were analyzed, but the result of only one case is presented here. The boundary condition is 0.1 MPa for the outlet pressure and 285.15 K for the inlet temperature. The average heat

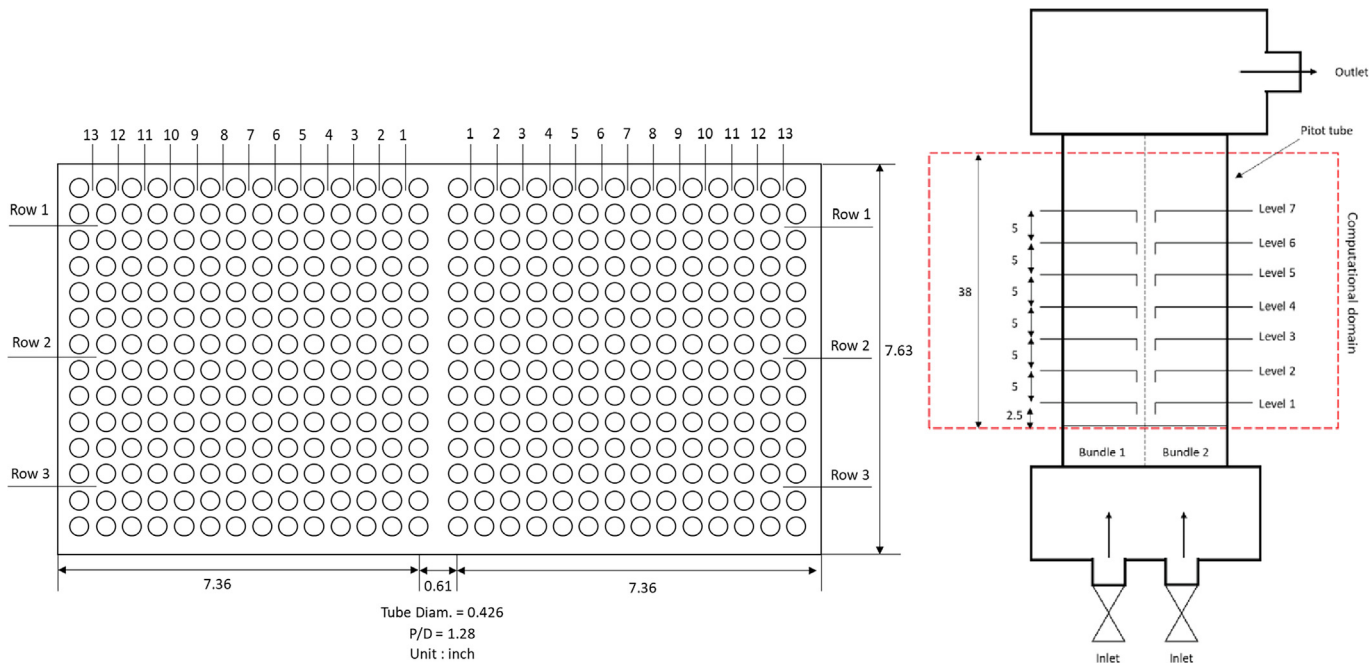


Fig. 10. Schematic diagrams of the Weiss two assembly test (left: Cross-sectional view, right: Longitudinal view).

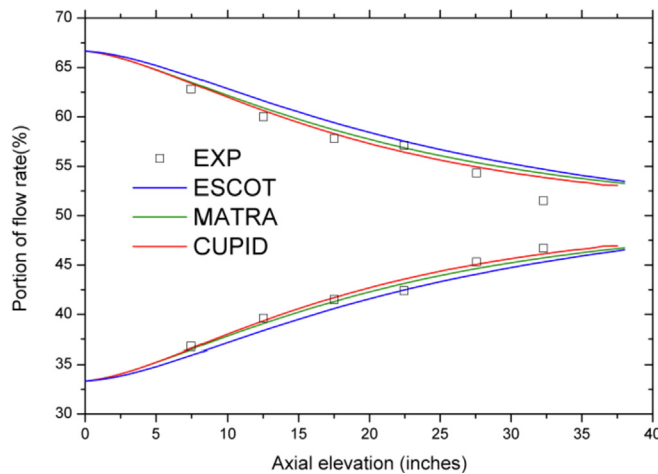


Fig. 11. Portion of assembly averaged flow rates in partial blockage case.

flux of a rod is 18.5 kW/m^2 and the power ratio between the hot and cold rods is 2:1. The turbulent mixing parameter β is set to 0.005 as in other codes.

The profiles of calculated temperatures and velocities at Windows 3 and 7 are shown in Fig. 16 and Fig. 17, respectively. The velocities are normalized by the inlet velocity. The flows in the hot regions are accelerated by the buoyancy effect. This acceleration is simulated properly by ESCOT. Although the differences between ESCOT and measurement are somewhat large, those are not particularly larger than the cases of CUPID and MATRA. The code-to-code comparison shown in Table 2 for the relative differences in temperature indicates that ESCOT matches better with CUPID than MATRA within 2% for all parameters.

3.2. Two-phase flow cases

3.2.1. RPI air-water test

The RPI air-water test was issued by NRC (Nuclear Regulatory Commission) and performed at Rensselaer Polytechnic Institute.

The purpose of this experiment was the investigation of the fully developed two-phase flow distribution in a 2×2 rod array test section. The flow is unheated. Fig. 18 shows a planar view sketch of the test section. The height of the test section is 914.4 mm without any spacer grid. Two techniques were used to mix water and air into the bundle: a mixing tee technique and a sinter section technique. The outlet void fraction at the corner, side, and center sub-channels were measured. Six tests were carried out with different boundary conditions: outlet pressure between 1.3 MPa and 2.8 MPa; inlet void fraction between 20% and 53%; the average inlet velocity of 0.451 or 0.903 m/s.

The computational model employs 90 meshes - 9 (3×3) radial meshes and 10 uniformly divided axial nodes. The complete Zuber & Findlay model is applied for the drift-flux parameters, and the EVVD model is activated with $\beta = 0.05$, $K_M = 1.4$, and $\Theta_M = 5.0$. Fig. 19 shows the predicted outlet void fraction versus the measured data for the mixing tee case (top) and the sinter section case (bottom). The effect of the void drift model is clearly demonstrated through the changes in the corner and center cells. The empty symbols represent the values obtained without the EVVD model. The void fractions at the corner are overestimated whereas those are underestimated at the center. When the EVVD model is activated, the effect of gathering small bubbles is reflected in the code so that the void fractions at the corner are lowered and ones at the center are increased. This results in a significant decrease of the difference from the measured data as shown in Table 3. Even though the differences from the measured data are still not small enough with the EVVD model, a similar level of differences are observed in the results of CUPID.

3.2.2. PSBT: phase 1-exercise 2

The PWR Subchannel and Bundle Test (PSBT) experiments include both single channel and rod bundle geometries under steady state and transient operating conditions. Here the test of Phase I-Exercise 2, which is the steady-state bundle benchmark, is selected for the validation of ESCOT to verify the void fraction prediction capability for bundle geometries.

The exercise involves numerous tests, and ESCOT solutions were

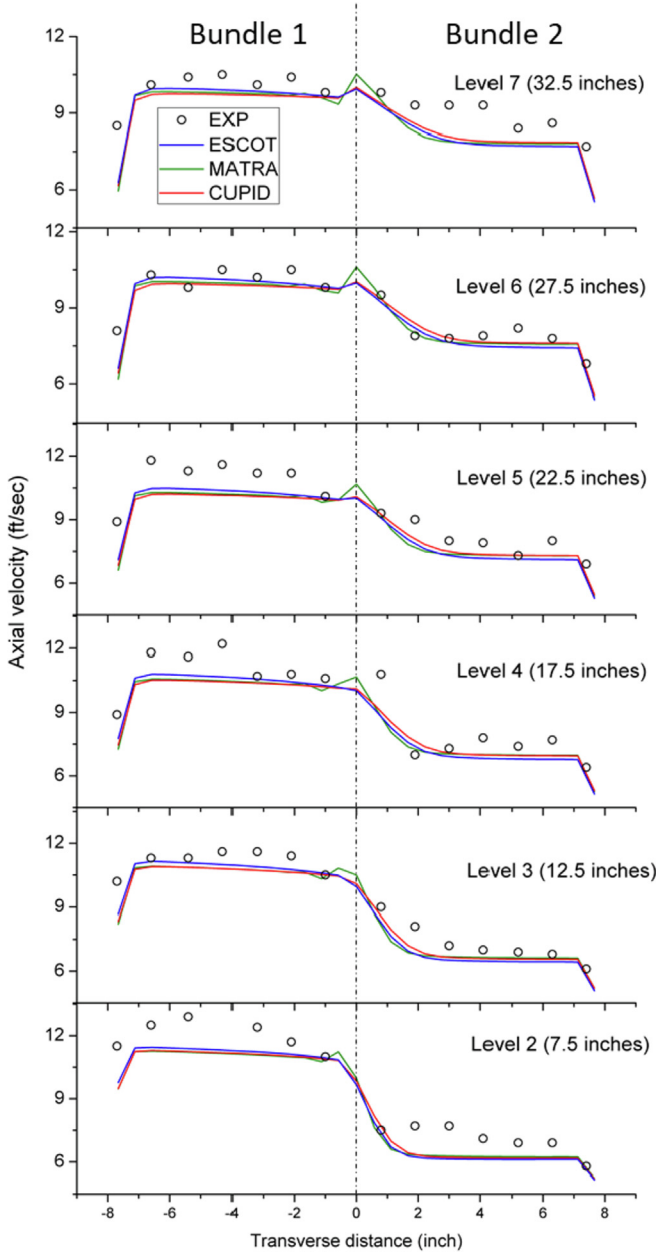


Fig. 12. Row averaged axial velocities at measured levels in partial blockage case.

obtained for Test Series 5, 6, and 7. The schematic diagram of the test facility is shown in Fig. 20. The test facility has 3658 mm heated length and three different types of spacer grids are installed: Mixing Vane (MV), No Mixing Vane (NMV) and Simple Spacer (SS). The form loss factors are set to 1.0, 0.7 and 0.4, respectively. Test Series 5 and 6 have the radial configuration shown in Fig. 20(A) while Test Series 7 has one unheated rod having a different diameter as illustrated in Fig. 20(B). The boundary conditions are given in wide ranges to the tests: pressure from 4.9 MPa to 16.5 MPa, average power from 1.0 to 3.5 MW, inlet temperature from 150 to 310 °C, and inlet mass flux from 2 to 11 kg/(m²s). The averaged void fraction in the four central channels surrounding the central rod or the averaged bundle void fraction is the quantity of interest in this steady state case. Three X-ray measurements were performed at three different heights: 2.216 m, 2.269 m and 3.177 m from the beginning of heated portion. The standard deviation of the void fraction measurement was 0.04.

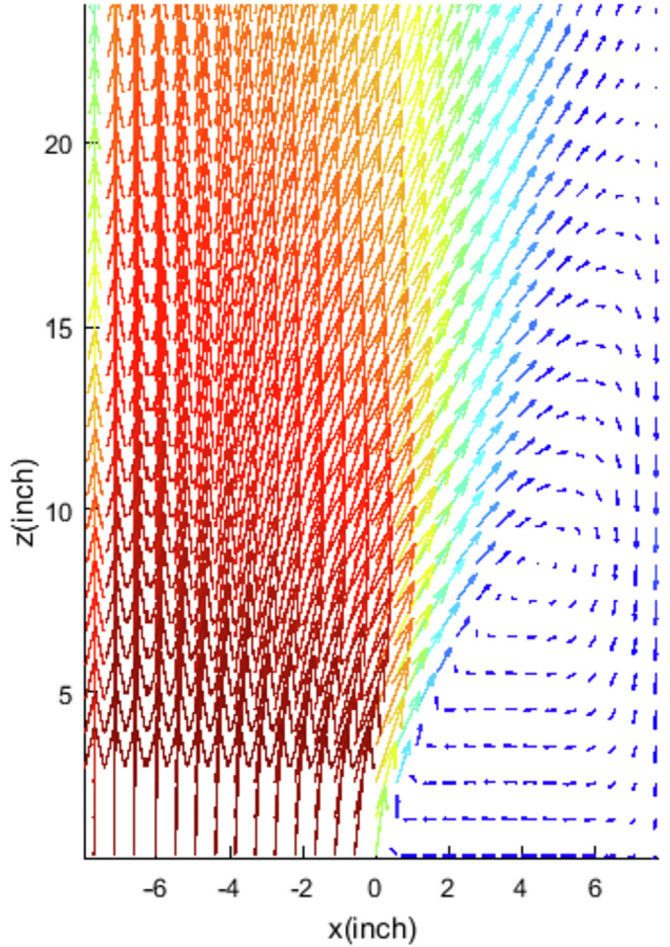


Fig. 13. Velocity vector map of the slice along the 2nd-Row line in full blockage case.

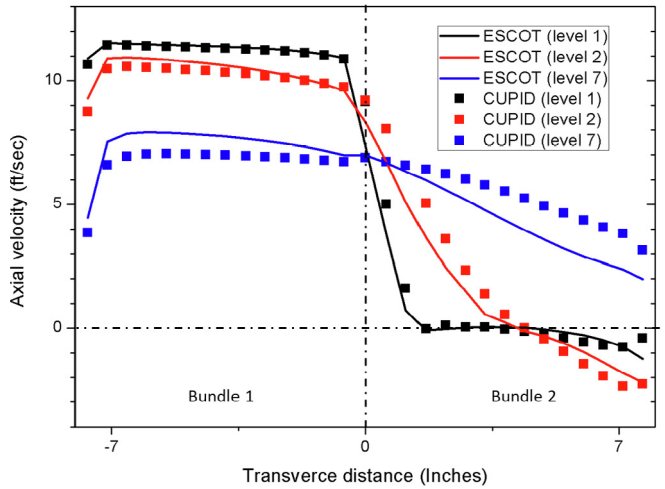


Fig. 14. Row averaged axial velocities in full blockage case.

In the ESCOT calculation, 36 subchannels are defined, and the axial meshes are non-uniformly set with 42 meshes for Test Series 5 and 6 while 79 meshes for Test Series 7. The Cheval-Lellouche model is applied for the drift-flux parameters, and the EVVD model is applied as $\beta = 0.05$, $K_M = 1.4$, and $\Theta_M = 5.0$. Fig. 21, Fig. 22, and Fig. 23 show the calculated void fractions compared to the measured data. It can be figured out that the ESCOT results agree

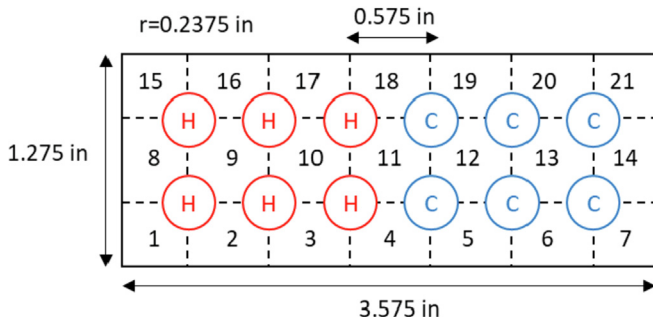


Fig. 15. Computational modeling of PNNL 2 × 6 test.

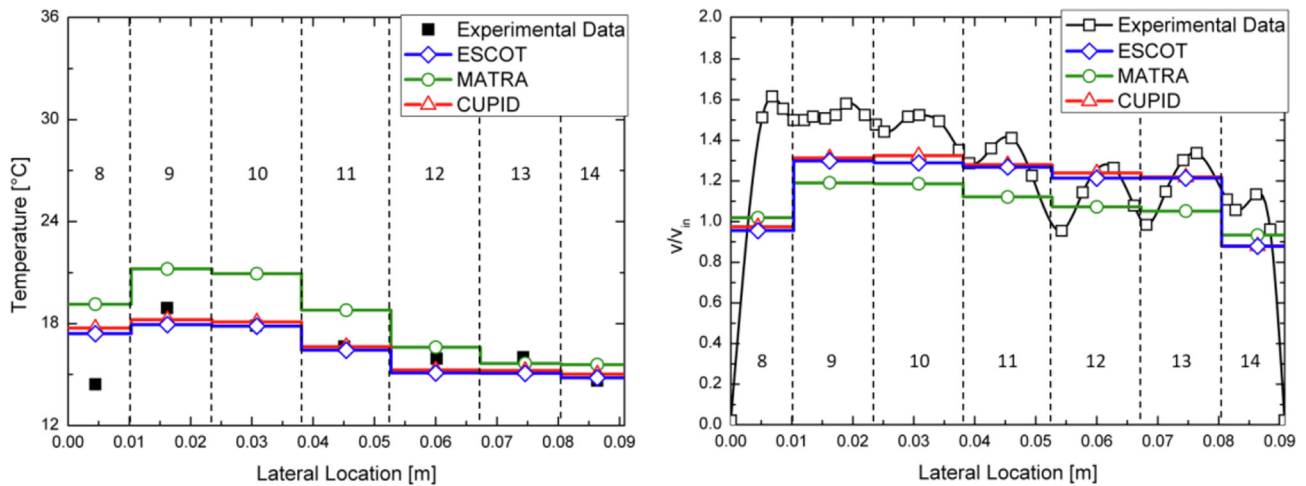


Fig. 16. Temperature and velocity profiles at window 3 of PNNL 2 × 6 case 1.

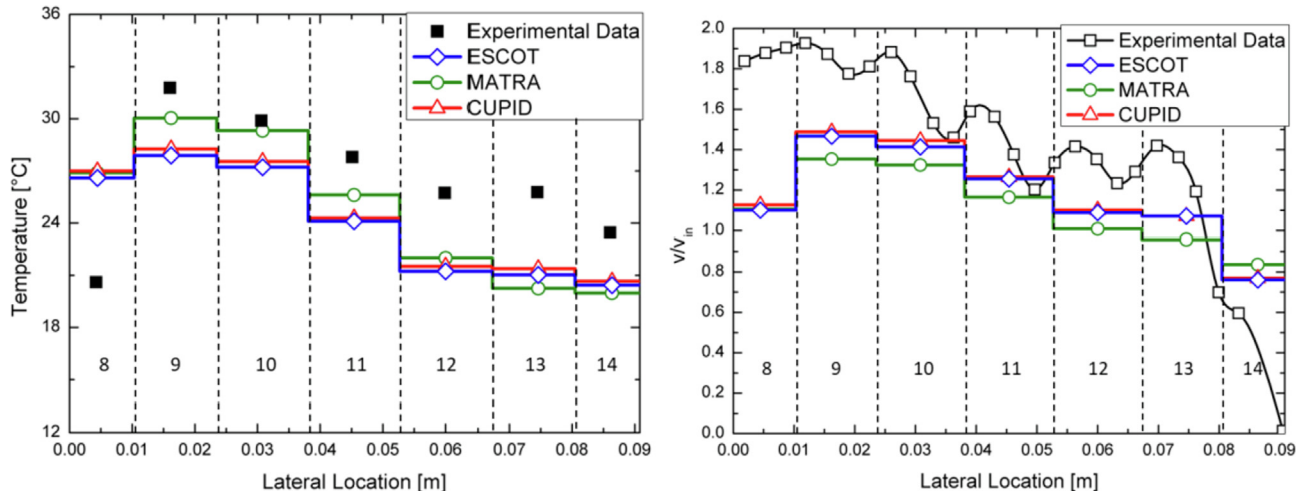


Fig. 17. Temperature and velocity profiles at window 7 of PNNL 2 × 6 case 1.

Table 2

Relative differences of ESCOT values from CUPID and MATRA values for PNNL 2 × 6 case 1.

	Max. [%]	Temperature		Velocity	
		Window 3	Window 7	Window 3	Window 7
ESCOT – CUPID		1.82	1.64	2.71	2.29
	RMS [%]	1.39	1.28	1.58	1.47
ESCOT – MATRA	Max. [%]	15.46	7.18	15.43	11.81
	RMS [%]	10.80	4.95	10.80	8.13

with the measured data within a 2σ band. The absolute differences in void fraction are summarized Table 4 which includes the CTF results given for comparison. It is noted that the magnitude of the difference of ESCOT is comparable with that of CTF.

4. Performance examination for PWR core problems

In order to examine the execution performance of ESCOT for real core problems, a reduced sized whole core (RSWC) problem and a quarter core OPR1000 problem are solved. The parallel performance is assessed for these two problems. Comparison with CTF is given for the first problem.

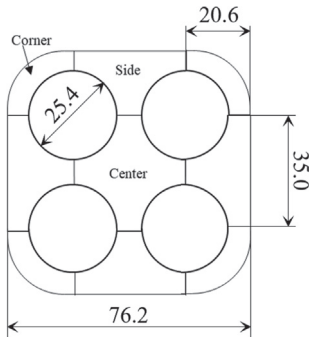


Fig. 18. Test Section of RPI Air Water Test (Numbers in mm).

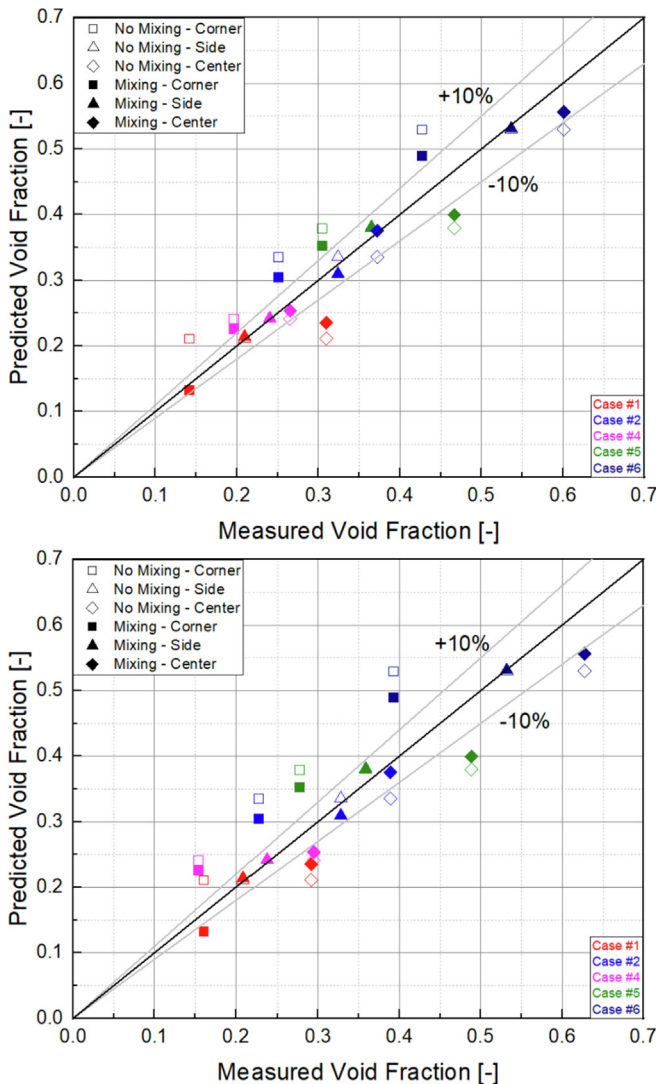


Fig. 19. Results for RPI air water test for mixing tee (top) and sinter section (bottom) cases.

4.1. Reduced size whole core problem

The RSWC consists of 89 fuel assemblies as shown in Fig. 24. There are 20 unheated rods in the 16×16 fuel assembly to represent the guide tubes of the Combustion Engineering (CE)-type-assembly. The choice of 89 assemblies is dictated by the number of the available processors on the test platform which is

Table 3
Differences in void fraction obtained without and with EVVD model for RPI test.

Mixing Tee	No Mixing			Mixing			
	Corner	Side	Center	Corner	Side	Center	
ESCOT	Max. [%]	49.5	4.03	31.8	21.8	4.49	24.0
	RMS [%]	32.7	2.50	18.3	15.7	3.03	13.1
CUPID	Max. [%]	62.0	20.3	25.8	44.3	21.4	22.3
	RMS [%]	42.4	12.3	14.7	21.4	13.9	13.6
Sinter Section	No Mixing			Mixing			
	Corner	Side	Center	Corner	Side	Center	
ESCOT	Max. [%]	57.1	5.8	27.5	47.3	6.21	19.3
	RMS [%]	42.8	2.9	20.1	31.8	4.02	14.4
CUPID	Max. [%]	69.0	19.8	23.0	36.1	20.9	20.1
	RMS [%]	49.0	12.0	16.5	26.4	13.6	14.5

120. Note that adding one more ring would require more than 120 fuel assemblies. The operating conditions for this problem are given in Table 5. The axial power profile takes a cosine shape, and the radial power distribution of assemblies is assigned as Fig. 24 while the pin power within each assembly is assumed uniform.

For the execution performance comparison, the model problem was solved by both ESCOT and CTF. The calculation conditions of both codes are given in Table 6. The number of subchannels is 23,137 and the active height of 3.8 m is uniformly divided into 40 nodes so that 925,480 computational meshes are used. The turbulent mixing parameter β is set to 0.05. The convergence of the pseudo steady-state can be determined by monitoring parameters related to balance and storage during a null-transient simulation. Domain decomposition is done only in the radial direction by assigning one processor to each assembly in order to be consistent with CTF.

The number of outer iterations turned out to be 114 and 215 in ESCOT and CTF, respectively, while the simulation times are 0.94 s and 1.11 s. The distributions of density and temperature are given in Fig. 25. The relative difference is calculated by subtracting the CTF value from the ESCOT value and dividing it by the CTF value. The maximum differences in density and temperature are 0.22% and 0.56% respectively, which shows quite good agreement in the code-to-code comparison.

The computing times are listed in Table 7. The single processor calculation takes 45 min and solving pressure equation is the most time-consuming part as it takes 41% of the total computing time. For the parallel execution of ESCOT, 89 processors are used. Except for the initialization process, the overall calculation process is well-parallelized so that the calculation could be finished in 50 s with a speedup of 53 yielding the parallel efficiency of 60%. The calculation times for updating the matrix elements and the source terms of CTF include the time to calculate the Heat Transfer Coefficient (HTC); to solve the conduction equation; to set up the continuity and energy equations; and to calculate the interfacial area. The total computing time of ESCOT is shorter than CTF by 1.5 times and it mainly results from a significant time reduction of solving the momentum equation. It proves the effectiveness of the DFM which is based on the mixture velocity rather than phasic velocities.

4.2. OPR1000 quarter core problem

The feature of bidirectional domain decomposition in ESCOT is a capability currently unavailable in other subchannel codes. An OPR1000 quarter core problem is used to demonstrate the bidirectional domain feature involving both axial and radial decomposition. The number of radial subdomains is 52 of which 37 are full fuel assemblies, 14 are half-sized assemblies, and 1 is a quarter-

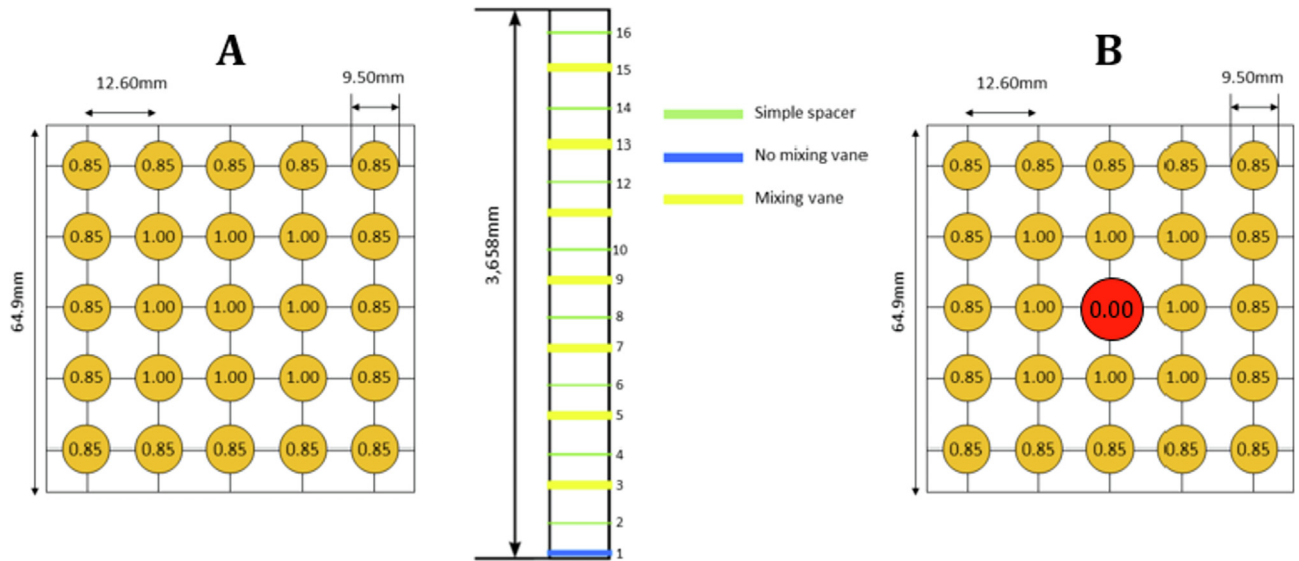


Fig. 20. Test sections of PSBT phase 1 exercise 2.

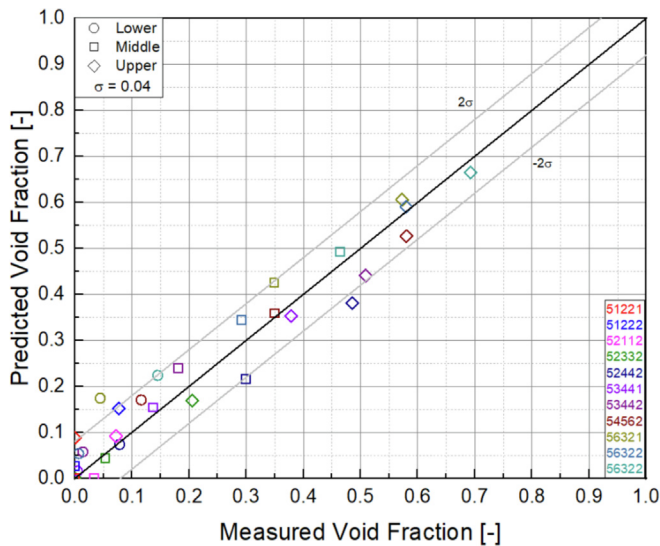


Fig. 21. Void fraction results for test series 5 of PSBT

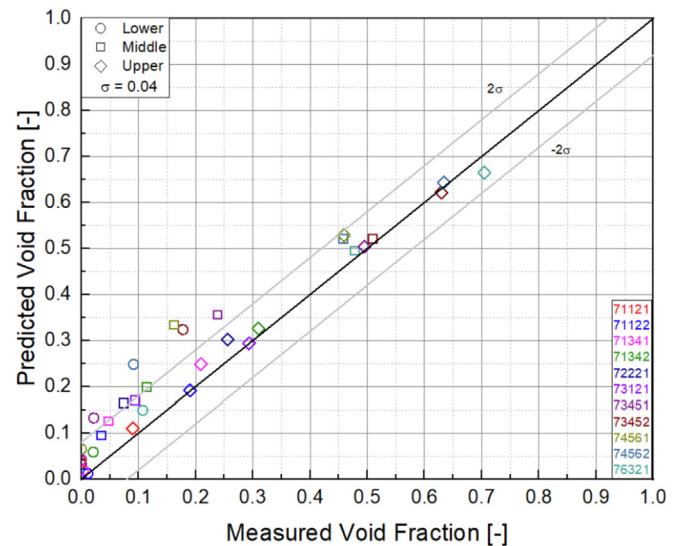


Fig. 23. Void fraction results for test series 7 of PSBT

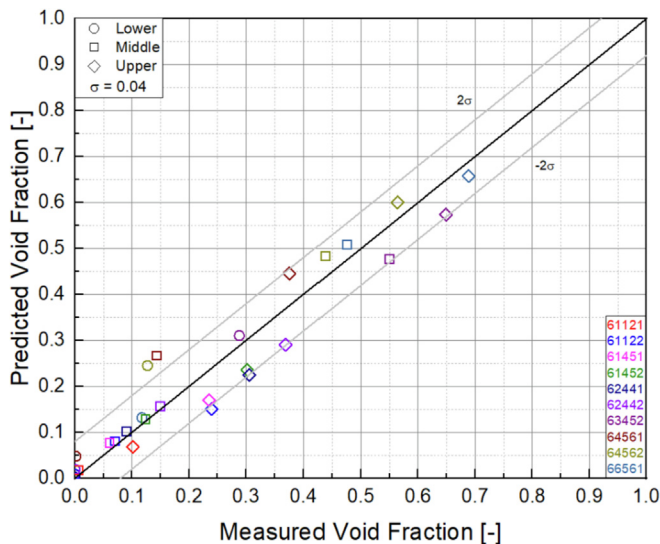


Fig. 22. Void fraction results for test series 6 of PSBT

sized. The total number of subchannels is 11,569 and the active core is non-uniformly subdivided into 32 planes to yield 370,208 computational meshes. The quarter core pin power distribution shown in Fig. 26 was provided by the nTRACER direct whole core calculation. The domain was first decomposed only axially and then radial decomposition was added at the second step. The detail calculation conditions are given in Table 8.

Fig. 27 illustrates the results of parallel executions. The axial-only decomposition reveals low parallel efficiency because the communication loads are increased in proportion to the number of channels in the core. Moreover the axial-only domain decomposition is bounded by the number of planes. The uneven size of radial subdomains deteriorates the parallel efficiency of the radial decomposition, but the scalability of the combined radial and axial decomposition is significantly better than the axial-only decomposition.

Consequently, the computing time is reduced from 1422 s—29 s with 104 processors.

Table 4

Absolute difference in void fraction at measured points for PSBT.

abs ($\Delta\alpha$)		Series 5			
		Lower	Middle	Upper	Total
ESCOT	Max.	0.130	0.083	0.105	—
	RMS	0.052	0.045	0.057	0.052
CTF	Max.	0.109	0.106	0.113	—
	RMS	0.036	0.045	0.069	0.051
		Series 6			
		Lower	Middle	Upper	Total
ESCOT	Max.	0.118	0.124	0.157	—
	RMS	0.042	0.049	0.066	0.053
CTF	Max.	0.185	0.073	0.092	—
	RMS	0.065	0.046	0.057	0.057
		Series 7			
		Lower	Middle	Upper	Total
ESCOT	Max.	0.157	0.172	0.070	—
	RMS	0.079	0.085	0.032	0.069
CTF	Max.	0.081	0.137	0.077	—
	RMS	0.032	0.072	0.042	0.052

5. Summary and conclusions

A new pin-level core T/H analysis code ESCOT was developed to achieve highly parallelized fast execution and efficient coupling with a high-fidelity neutronics code. The governing equations of ESCOT were based on the four-equation DFM and were discretized by the FVM. The SIMPLEC algorithm was applied to derive the pressure correction equation for the whole 3-D domain. Several constitutive relations were implemented to consider key physical phenomena such as turbulent mixing, void drift, pressure loss, and subcooled boiling. Parallelization was achieved by both radial and axial domain decomposition involving ghost cells.

The solution accuracy of ESCOT was verified with five sub-channel experiments which involved various key flow phenomena such as pressure drop by spacer grids, cross flow, flow reversal, void

Table 5

Operating conditions of reduced size whole core problem.

Parameter	Value
Inlet temp.	295.89 °C
Outlet pressure	15.513 MPa
Total inlet mass flow rate	7654.0 kg/sec
Assembly nominal power	15.904 MW

formation and mixing. ESCOT properly produced solutions which agreed with the experiments within the error bands that were comparable to other subchannel-scale codes such as CTF, MATRA, and CUPID. In particular, the results of two-phase flow validations demonstrated that DFM could predict solutions as well as the two-fluid model for the pre-CHF conditions.

The performance examination was carried out for two PWR core problems. The first one was the reduced size whole core problem for which a parallel efficiency of 60% was achieved with 89 processors. It turned out that ESCOT is 1.5 times faster than CTF, and this demonstrates that the use of the DFM is advantageous because the computing time to solve the momentum equations can be seriously reduced. For the second problem, the quarter core of an OPR1000, combined axial and radial domain decomposition was also tested and it turned that a steady-state can be reached within 30 s with 104 processors for the entire core pin level subchannel calculation.

The performance of ESCOT can be improved further using an optimized steam stable. The second heaviest load in ESCOT is represented by the time for updating variables of the next time step, and it is strongly relying on reading the steam table. The ASME steam table could be a good replacement of the IAPWS steam table since the CTF performance is enhanced by a factor two with the ASME steam table. Secondly, the characteristic of the linear system of the pressure equation has to be optimized. The computing time for solving the pressure equation takes significantly longer in ESCOT than in CTF. Numerous ways to derive an efficient pressure equation have been suggested [40] so that ESCOT can be improved

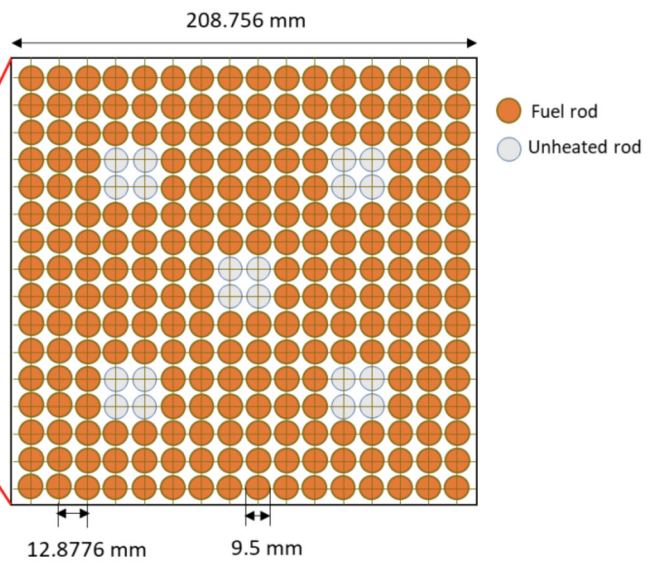


Fig. 24. Core power distribution and assembly geometry for reduced-size whole core problem.

Table 6
Calculation conditions for reduced-size whole core problem.

	ESCOT	CTF
# of computational meshes	925,480 (23,137 × 40)	
Courant number	0.60	0.80
Linear solver	PETSc: unpreconditioned BiCGStab	
Convergence criteria	Mass/Energy balance [%] Mass/Energy storage [%]	0.01/0.01 0.5/0.5 1 or 89
# of processors		1.0/5.0 89
Computing device		Intel Xeon E5-2630 v4 2.20 GHz/InfiniBand

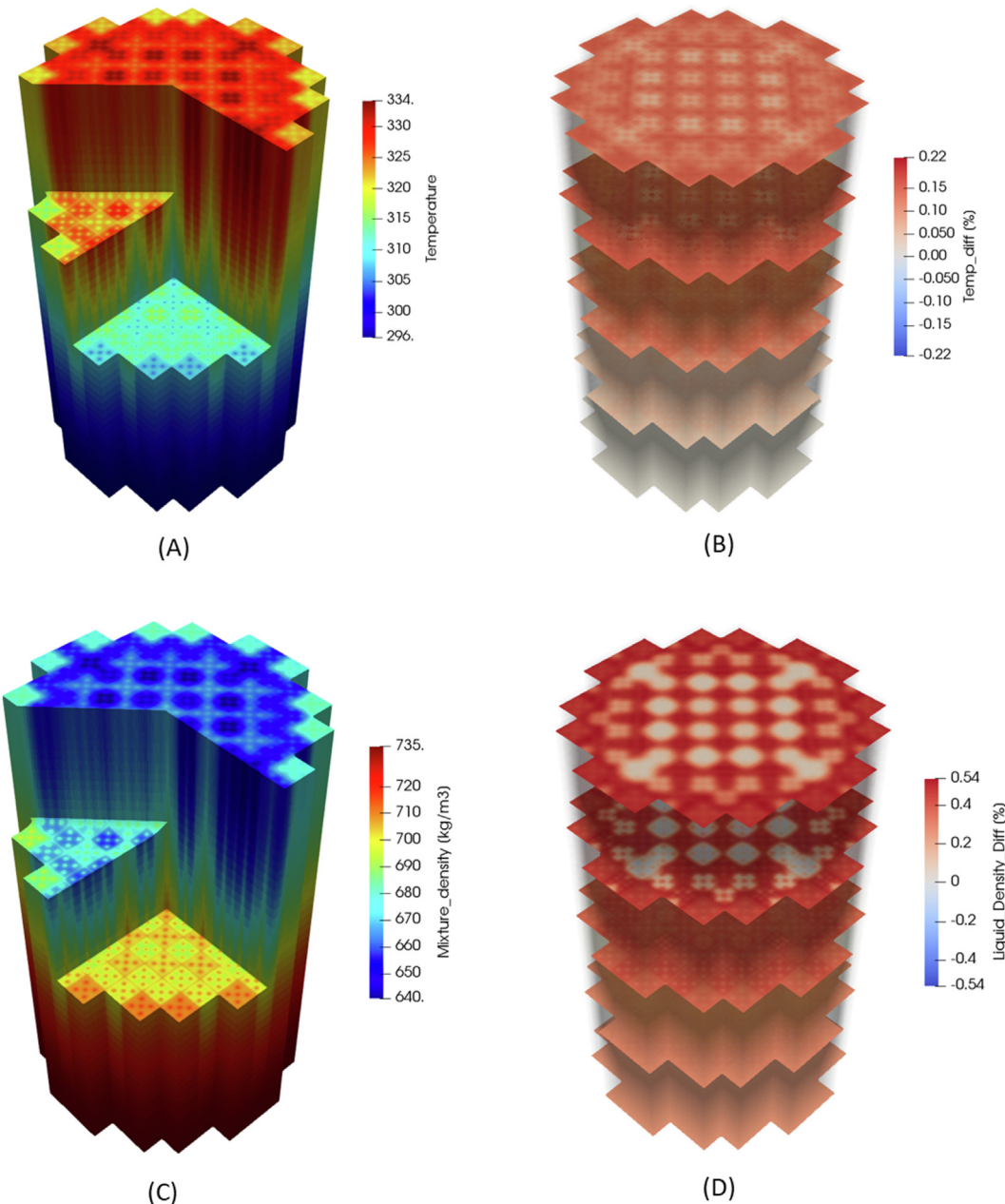


Fig. 25. Distributions of ESCOT Results and Relative Differences from CTF.
(A) Temperature; (B) Temperature relative difference; (C) Density; (D) Density relative difference.

by utilizing those ideas trying to decrease the condition number of the pressure matrix.

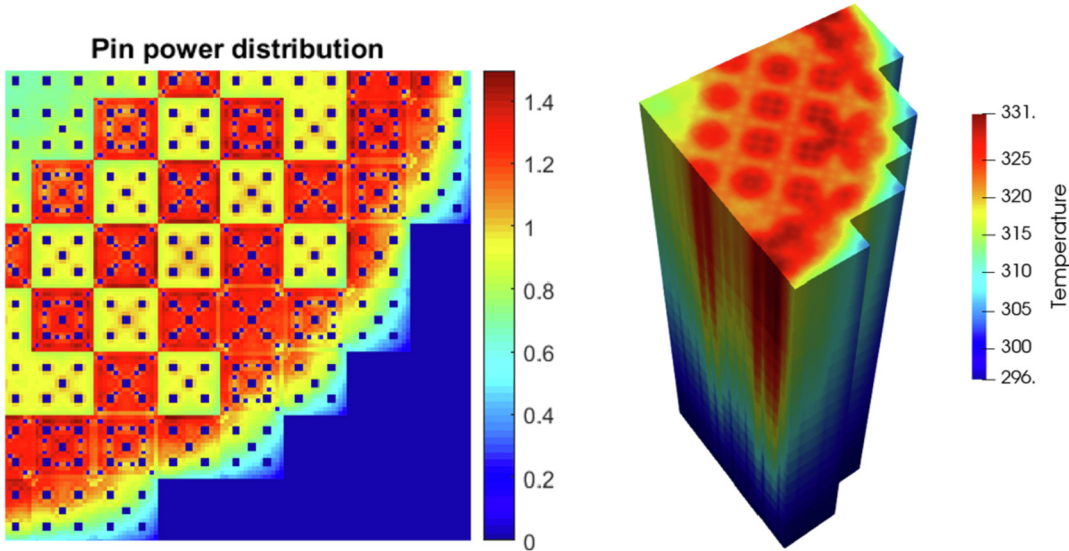
An in-depth examination of the parallel performance of ESCOT against various problem sizes is planned. Establishing a platform

for pin-level neutronics - T/H coupled calculations is also one of the main future work. Moreover, the validation of ESCOT on transient conditions is in order as well.

Table 7

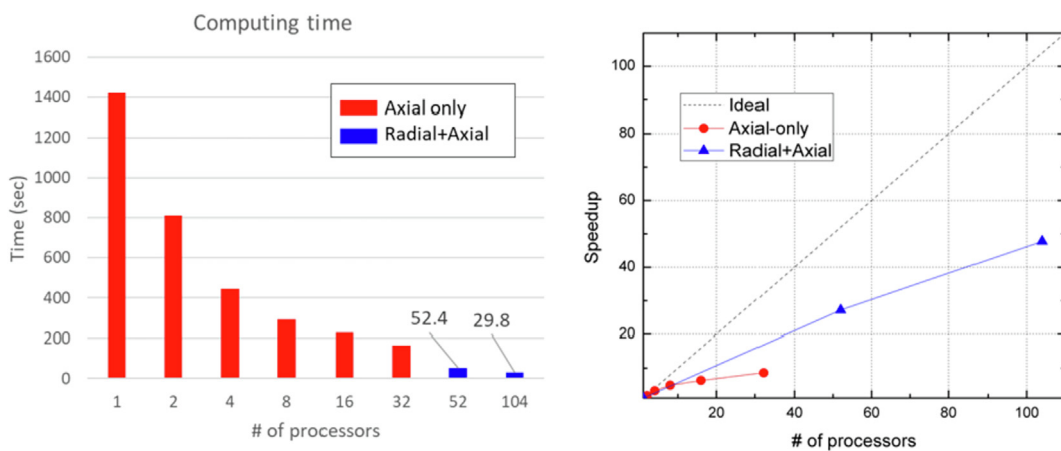
Computing time and speedup for reduced size whole core problem.

	Single processor Computing time (sec)	ESCOT			CTF Parallel computing time (sec)
		Computing time (sec)	Speedup	efficiency	
Initialization	7.2	5.1	1.41	0.02	4.6
Matrix elements update	531.0	8.0	66.79	0.75	27.0
Source terms update	276.3	3.5	78.06	0.88	
Solving momentum equation	86.9	2.0	44.32	0.50	30.3
Solving pressure equation	1110.7	17.5	63.62	0.71	6.4
Solving scalar variables	18.0	0.9	19.32	0.22	—
Updt. next time step vars.	647.6	13.4	48.18	0.54	5.3
whole simulation time	2677.7	50.4	53.15	0.60	73.6

**Fig. 26.** nTRACER Axially Averaged Radial Pin Power Distribution (left) and ESCOT Calculated Coolant Temperature (right) for OPR1000 Quarter Core Problem.**Table 8**

Calculation conditions for OPR10000 quarter core problem.

	Calculation conditions
# of computational meshes	370,208 (11,569 × 32)
Courant number	0.60
Linear solver	PETSc: Block Jacobi preconditioned BiCGStab
Convergence criteria	Mass/Energy balance [%] Mass/Energy storage [%]
# of processors	0.01/0.01 0.5/0.5 1, 2, 4, 8, 16, 32 52, 104
Computing device	Intel Xeon E5-2630 v4 2.20 GHz/InfiniBand

**Fig. 27.** Computing time (left) and scalability (right) of different domain decomposition schemes for OPR1000 quarter core problem.

Acknowledgments

This work was supported by Korea Atomic Energy Research Institute (KAERI) and funded by Korea Hydro and Nuclear Power Central Research Institute (KHNP CRI). Authors want to thank PETSc team and CTF, MATRA and CUPID teams for having shared their data for a solid comparison between the subchannel codes SNURPL has access.

References

- [1] B. Kochunas, et al., VERA core simulator methodology for pressurized water reactor cycle depletion, *Nucl. Sci. Eng.* 185 (2017).
- [2] M. Christienne, et al., Coupled TORT-TD/CTF capability for high-fidelity LWR core calculations, in: PHYSOR 2010, 2010, Pittsburgh, PA, USA.
- [3] J. Lee, et al., nTRACER/COBRA-TF coupling and initial assessment, in: Proc. Of the KNS 2015, Spring, Jeju, Rep. of Korea, 2015.
- [4] J.A. Turner, et al., The virtual environment for reactor applications (VERA). Design architecture, *J. Comput. Phys.* 326 (2016) 544–568.
- [5] V. Seker, et al., Reactor simulation with coupled Monte Carlo and computational fluid Dynamics, in: Joint International Topical Meeting on Mathematics & Computation and Supercomputing in Nuclear Applications (M&C + SNA 2007), 2007, Monterey, California, USA.
- [6] R. Tuominen, et al., Coupling SERPENT and OPENFOAM for neutronics-CFD multi-physics calculations, in: Proc. Of PHYSOR, 2016, Sun Valley, ID, USA, 2016.
- [7] R. Salko, M. Avramova, COBRA-TF Subchannel Thermal-Hydraulics Code (CTF) Theory Manual-Revision 0, The Pennsylvania State University, 2015.
- [8] S. Patankar, Numerical Heat Transfer and Fluid Flow, CRC press, 1980.
- [9] MPACT TEAM, Consortium for Advanced Simulation of Light Water Reactors, 2015. MPACT Theory Manual v2. 1.0.
- [10] A. Seubert, K. Velkov, S. Langenbuch, The time-dependent 3D discrete ordinates code TORT-TD with thermal-hydraulic feedback by ATHLET models, in: PHYSOR 2008, Interlaken, Switzerland, 2008.
- [11] Y.S. Jung, et al., Practical numerical reactor employing direct whole core neutron transport and subchannel thermal/hydraulic solvers, *Ann. Nucl. Energy* 62 (2013) 357–374.
- [12] H.Y. Yoon, et al., CUPID Code Manual Volume I: Mathematical Models and Solution Methods, Korea Atomic Energy Research Institute, 2011.
- [13] S.J. Yoon, et al., Application of CUPID for subchannel-scale thermal-hydraulic analysis of pressurized water reactor core under single-phase conditions, *Nucl. Eng. Technol.* 50 (2018) 54–67.
- [14] J.R. Lee, H.Y. Yoon, Multi-physics approach for nuclear reactor analysis using thermal-hydraulics and neutron kinetics coupling methodology, in: Tenth International Conference on Computational Fluid Dynamics, 2018, Barcelona, Spain.
- [15] H. Kwon, et al., Validation of a Subchannel Analysis Code MATRA Version 1.1, Korea Atomic Energy Research Institute, 2014. KAERI/TR-5581/2014.
- [16] S. Kim, et al., Preliminary coupling of MATRA code for multi-physics analysis, in: Proc. Of the KNS 2014 Spring Meeting, Jeju, Rep. of Korea, 2014.
- [17] C.B. Shim, et al., Cross flow modeling in direct whole core transport calculation with a subchannel solver, in: Proc. ICAPP 2013, Jeju, Rep. of Korea, 2013.
- [18] N. Zuber, J. Findlay, Average volumetric concentration in two-phase flow systems, *J. Heat Transf.* 87 (4) (1965) 453–468.
- [19] M. P. Paulsen et al., "RETRAN-3D—A Program for Transient Thermal-Hydraulic Analysis of Complex Fluid Flow Systems Volume vol 3: User's Manual," NP-7450.
- [20] Y.J. Chung, et al., Development and assessment of system analysis code, TASS/SMR for integral reactor, SMART, *Nucl. Eng. Des.* 244 (2012) 52–60.
- [21] L. Wolf, L.J.M. Guillebaud, A. Faya, WOSUB: a Subchannel Code for Steady-State and Transient Thermal-Hydraulic Analysis of BWR Fuel Pin Bundles, Energy Laboratory, Massachusetts Institute of Technology, 1978.
- [22] M.B. Carver, et al., Simulation of the distribution of flow and phases in vertical and horizontal bundles using the ASSERT-4 subchannel code, *Nucl. Eng. Des.* 122 (1990) 413–424.
- [23] B. Chexal, et al., A void fraction correlation for generalized applications, *Prog. Nucl. Energy* 27 (4) (1992) 255–295.
- [24] N.E. Todreas, M.S. Kazimi, Nuclear Systems Volume I: Thermal Hydraulic Fundamentals, CRC press, 2011.
- [25] A.A. Armand, The Resistance during the Movement of a Two-phase System in Horizontal Pipes, Izvestia Vsesoiuznogo Teplotekhnicheskogo Instituta, 1946.
- [26] J.E. Kelly, S.P. Kao, M.S. Kazimi, THERMIT-2: A Two-Fluid Model for Light Water Reactor Subchannel Transient Analysis, MIT Energy Laboratory Electric Utility Program, 1981. MIT-EL-81-014.
- [27] S.G. Beus, Two-Phase Turbulent Mixing Model for Flow in Rod Bundles, Bettis Atomic Power Lab., Pittsburgh, 1972. No. WAPD-T-2438.
- [28] T. R.-3. C.D. Team, RELAP5-3D Code Manual Volume IV: Models and Correlations, Idaho National Engineering and Environmental Laboratory, 2002. INEEL-EXT-98-00834.
- [29] R.T. Lahey, A mechanistic subcooled boiling model, in: Proc. Of the 6th Int. Heat Transfer Conference, 1978.
- [30] J.P. Van Doormaal, G.D. Raithby, Enhancement of the SIMPLE method for predicting incompressible fluid flows, *Numer. Heat Tran. 7 (2)* (1984) 147–163.
- [31] M. Mohitpour, G. Jahanfarnia, M. Shams, An advancement in iterative solution schemes for three-dimensional, two-fluid modeling of two-phase flow in PWR fuel bundles, *Ann. Nucl. Energy* 63 (2014) 83–99.
- [32] PETSc Team, PETSc Users Manual, Argonne National Laboratory, 2018. ANL-95/11 - Rev. 3.10.
- [33] R.K. Salko, R.C. Schmidt, M.N. Avramova, Optimization and parallelization of the thermal–hydraulic subchannel code CTF for high-fidelity multi-physics applications, *Ann. Nucl. Energy* 84 (2015) 122–130.
- [34] R. Salko, et al., CTF Validation, CASL, 2016. CASL-U-2016-1113-000.
- [35] V. Marinelli, L. Pastori, B. Kjellen, Experimental Investigation of Mass Velocity Distribution and Velocity Profiles in an LWR Rod Bundle, American Nuclear Society, Rome, Italy, 1972. Trans.
- [36] E. Weiss, R.A. Markley, A. Battacharyya, Open duct cooling-concept for the radial blanket region of a Fast Breeder reactor, *Nucl. Eng. Des.* 16 (4) (1971) 375–386.
- [37] J.M. Bates, E.U. Khan, Investigation of combined free and forced convection in a 2x6 rod bundle during controlled flow transients, PNL- 3135 (1980).
- [38] R.W. Sterner, R.T. Lahey Jr., Air/water Subchannel Measurements of the Equilibrium Quality and Mass-Flux Distribution in a Rod bundle[BWR], Rensselaer Polytechnic Inst., 1983. No. NUREG/CR-3373.
- [39] A. Rubin, et al., OECD/NRC Benchmark Based on NUPEC PWR Subchannel and Bundle Tests (PSBT), Volume I: Experimental Database and Final Problem Specifications, Nuclear Energy Agency, 2010. US NRC OECD.
- [40] H.Y. Yoon, J.J. Jeong, A continuity-based semi-implicit scheme for transient two-phase flows, *J. Nucl. Sci. Technol.* 47 (9) (2010) 779–789.